Effects of thermal annealing on C/FePt granular multilayers: *in situ* and *ex situ* studies

2008 J. Phys.: Condens. Matter 20 035218

(http://iopscience.iop.org/0953-8984/20/3/035218)

IOP Publishing Journal of Physics: Condensed Matter

J. Phys.: Condens. Matter **20** (2008) 035218 (10pp) doi:10.1088/0953-8984/20/03/035218

Effects of thermal annealing on C/FePt granular multilayers: *in situ* and *ex situ* studies

D Babonneau[1], G Abadias[1], J Toudert[1,5], T Girardeau[1], E Fonda[2], J S Micha[3] and F Petroff[4]

[1] Laboratoire de Métallurgie Physique, UMR 6630 CNRS, Université de Poitiers, SP2MI,
Téléport 2, Boulevard M et P Curie, BP 30179, 86962 Futuroscope Chasseneuil Cedex, France
[2] Synchrotron SOLEIL, L'Orme des Merisiers, St-Aubin, BP 48, 91192 Gif-sur-Yvette Cedex,
France
[3] UMR SPrAM 5819 CNRS, CEA-Grenoble/DRMFC, 17 avenue des martyrs,
38054 Grenoble Cedex 9, France
[4] Unité Mixte de Physique CNRS/THALES associée à l'Université Paris-Sud XI,
Route départementale 128, 91767 Palaiseau Cedex, France

E-mail: david.babonneau@univ-poitiers.fr

Received 10 October 2007
Published 19 December 2007
Online at stacks.iop.org/JPhysCM/20/035218

Abstract

The comprehensive study of C/FePt granular multilayers prepared by ion-beam sputtering at room temperature and subsequent annealing is reported. The as-deposited multilayers consist of carbon-encapsulated FePt nanoparticles (average size ∼3 nm) with a disordered face-centered-cubic structure. The effects of thermal annealing on the structural and magnetic properties are investigated by using dedicated *ex situ* and *in situ* techniques, including high-resolution transmission electron microscopy, extended x-ray absorption fine structure, magnetometry, and coupled grazing incidence small-angle x-ray scattering and x-ray diffraction. Our structural data show that the particle size and interparticle distance increase slightly with annealing at temperatures below 790 K by thermally activated migration of Fe and Pt atoms. We find that thermal annealing at temperatures above 870 K results in the dramatic growth of the FePt nanoparticles by coalescence and their gradual $L1_0$ ordering. In addition, we observe a preferential graphitization of the carbon matrix, which provides protection against oxidation for the FePt nanoparticles. Magnetization measurements indicate that progressive magnetic hardening occurs after annealing. The dependences of the blocking temperature, saturation magnetization, coercivity, and magnetocrystalline anisotropy energy on the annealing temperature are discussed on the basis of the structural data.

(Some figures in this article are in colour only in the electronic version)

1. Introduction

Nanoscale magnetic systems are attracting considerable attention due to their potential in the field of ultrahigh density magnetic recording media [1]. To achieve high storage densities beyond 1 Tbit in^{-2}, assemblies of ferromagnetic monodomain particles with uniform and small size below 10 nm are required. However, as the magnetic bit size is further reduced to the superparamagnetic limit, the magnetization of the particles is easily perturbed by thermal agitation. In order to overcome superparamagnetism, recent studies have been focused on CoPt and FePt nanoparticle arrays owing mainly to the existence of chemically ordered phases with exceptional magnetic properties such as large magnetocrystalline anisotropy constant above 10^7 erg cm^{-3} [2, 3]. Additional requirements for future magnetic recording media are that the nanoparticles have to be magnetically isolated but also chemically and mechani-

---

[5] Present address: Instituto de Óptica 'Daza de Valdés' (CSIC), Serrano 121, 28006 Madrid, Spain.

cally stable. Therefore, much research has been done on granular thin films consisting of CoPt and FePt nanoparticles embedded in various nonmagnetic matrices [4–23]. Among the prospective materials, C/CoPt and C/FePt granular thin films have attracted great interest [18–23] because carbon not only impedes the growth of the nanoparticles, but also provides protection against outside degradations and reduces interparticle exchange interactions [24, 25].

In general, CoPt and FePt nanoparticles in carbon-based granular films fabricated by sputtering processes at low substrate temperature have a disordered face-centered-cubic (fcc) structure (A1 phase), which is magnetically soft. In order to transform the as-deposited nanoparticles into the ordered face-centered-tetragonal (fct) structure ($L1_0$ phase), post-annealing at temperatures above 770 K is necessary. Hence, it is predicted that the control of the magnetic properties of these granular thin films should be possible by adjusting the film composition, annealing temperature, and duration. However, concurrently with chemical ordering, thermal treatment also causes particle growth and coalescence, which may adversely affect the magnetic properties. Structural changes during the annealing process are therefore one of the key issues for future applications. There is also some fundamental interest concerning the kinetics of particle growth and chemical ordering associated with thermal enhancement of the atomic mobility. A lot of studies on FePt-based granular systems have been carried out in order to highlight the mechanisms responsible for the thermal evolution of the structural parameters. The results have been discussed on the basis of *ex situ* transmission electron microscopy (TEM), x-ray diffraction (XRD), and small-angle neutron and x-ray scattering (SANS, SAXS) experiments [9, 20, 26–28]. However, these mechanisms remain unclear and microstructural investigations of such systems by *in situ* measurements are scarce.

In the present article we focus on C/FePt granular multilayers grown by alternate ion-beam sputtering and post-annealed in vacuum. We investigate in detail the structural and magnetic properties of the as-deposited and post-annealed granular films by combining various *ex situ* techniques, including high-resolution TEM (HRTEM), XRD, grazing incidence SAXS (GISAXS), extended x-ray absorption fine structure (EXAFS), and superconducting quantum interference device (SQUID) magnetometry. Besides, in order to complete the physical description of the thermal annealing effects, we have studied the morphological and crystallographic evolution of the FePt nanoparticles by performing coupled *in situ* GISAXS and grazing incidence XRD (GIXRD) experiments.

2. Experimental details

$(C/FePt)_N$ multilayers were fabricated at room temperature (RT) by alternate ion-beam sputtering deposition of C and FePt layers on surface oxidized Si(001) substrates. The base pressure in the deposition chamber was 2×10^{-8} Torr and the sputtering process was carried out at 2×10^{-4} Torr by using an Ar^+ ion-beam operated at 1.2 keV and 80 mA. The nominal thickness of the carbon and FePt layers was $t_C = 4.3$ nm and $t_{FePt} = 1.1$ nm, respectively, and the number of bilayers was $N = 20$ or 40. For all the films, an additional 10 nm carbon capping layer was sputtered at the end of the deposition process in order to prevent diffusion and oxidation of the last FePt layer under ambient conditions. The stoichiometry of the FePt layers was determined to be 1:1 by Rutherford backscattering spectrometry (RBS) [29].

The as-deposited multilayers with $N = 20$ were post-annealed in vacuum at different temperatures ranging from 770 to 1070 K and were characterized by various *ex situ* techniques. The microstructure was examined by cross-sectional HRTEM performed with a JEOL 3010 microscope equipped with a LaB_6 emitter and operated at 300 keV. Morphology and spatial organization of the FePt nanoparticles were studied by GISAXS carried out at the DW31B beamline of the LURE synchrotron facility (Orsay, France). The energy of the incident photons was fixed to 7 keV, the angle of incidence with respect to the surface was $\omega = 0.3°$ and the scattering was monitored in the (q_y, q_z) reciprocal space with a charge-coupled device (CCD) 2D detector located 0.380 m away from the sample. Magnetic properties were measured in the temperature range 5–370 K using a Quantum Design SQUID magnetometer with a magnetic field between ±50 kOe applied parallel to the plane of the films. The magnetization curves were corrected for the diamagnetic background signal of the substrate and of the carbon matrix by subtracting a linear function as determined from the slope of the magnetization data in the field range 35–50 kOe.

The multilayers with $N = 40$ were post-annealed in vacuum at 870 K for 1 h. Local structure around Fe and Pt atoms (i.e. interatomic distances, number and type of neighboring atoms) was investigated by EXAFS. Measurements at the Fe K and Pt L_3 edges were taken in the total electron yield mode at RT on the A1 beamline of HASYLAB at the DESY synchrotron facility (Hamburg, Germany). Chemical ordering of the FePt nanoparticles was also studied by XRD carried out at the CRG-IF BM32 beamline at the European Synchrotron Radiation Facility (ESRF, Grenoble, France). The sample was kept vertical during the course of the measurements and the incident wavelength was fixed to 0.11 nm. The diffracted intensities were measured with the scattering angle being varied from $2\theta = 10°$ to 62° in both Bragg–Brentano (θ–2θ) and grazing incidence ($\omega = 1°$) configurations. To probe in real-time the thermal evolution of the FePt nanoparticles, $(C/FePt)_{40}$ multilayers were subjected to *in situ* annealing under vacuum at 10^{-6} Torr in a temperature range from 610 to 1010 K on the BM32 beamline of the ESRF. GISAXS (CCD was placed at 0.815 m from the sample, $\omega = 0.3°$) and GIXRD (2θ-angular range was reduced to 26°–36° for steric reasons, $\omega = 1°$) measurements were completed successively while keeping the sample at constant temperature during the acquisitions.

3. Structure and spatial organization

3.1. *Ex situ HRTEM observations*

Figure 1 shows the microstructure of as-deposited and post-annealed $(C/FePt)_{20}$ multilayers. It is clearly seen that the

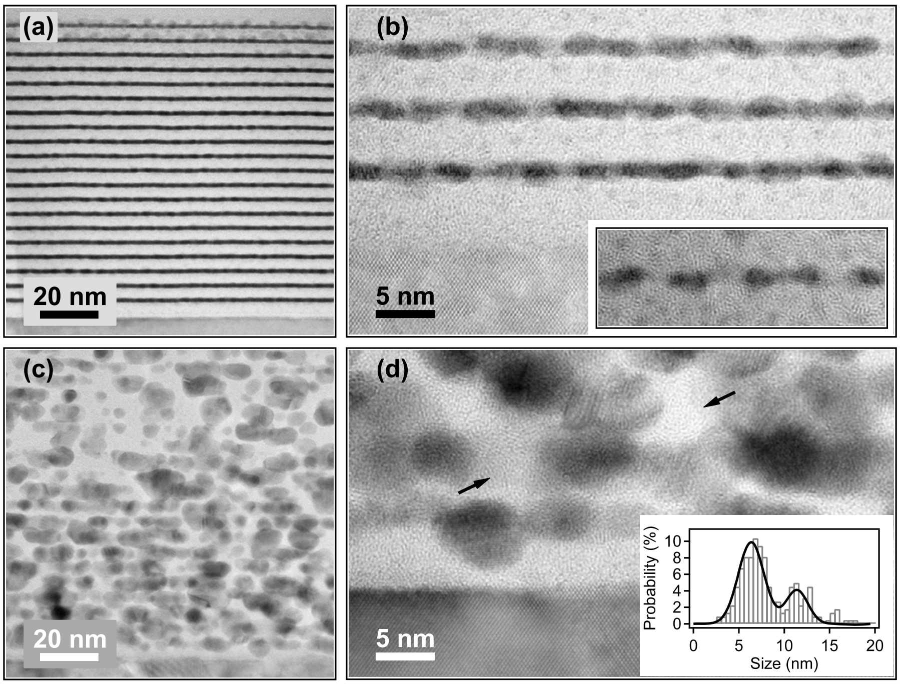

Figure 1. Microstructure of $(C/FePt)_{20}$ multilayers observed by low-magnification and high-resolution TEM cross-section. (a), (b) As-deposited specimen. The inset in (b) shows disconnected FePt nanoparticles observed in a zone of high electron-transparency. (c), (d) Specimen post-annealed at 1070 K for 1 h. The inset in (d) displays the size distribution of the annealed FePt nanoparticles. Arrows in (d) indicate the presence of graphite-like structures.

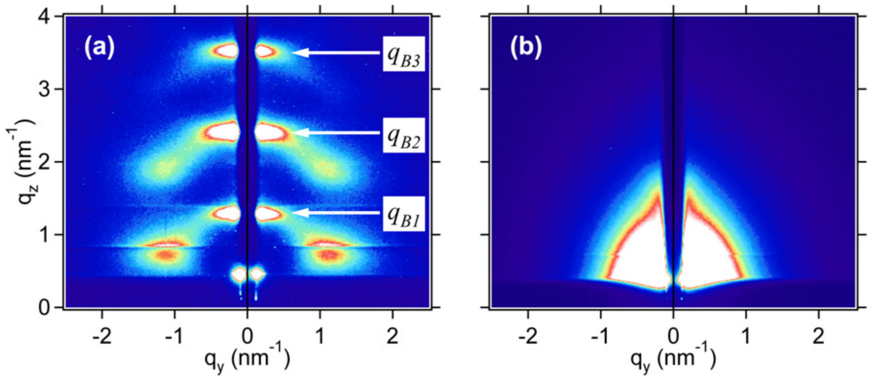

Figure 2. 2D GISAXS patterns of $(C/FePt)_{20}$ multilayers: (a) as-deposited and (b) post-annealed at 1070 K for 1 h.

alternate deposition of thin FePt layers and thicker carbon layers produces a layered structure (figure 1(a)), which appears as planes of dark FePt nanograins separated by amorphous carbon layers (figure 1(b)). The FePt nanograins have the shape of oblate spheroids with lateral diameter around 3 nm and aspect ratio (height/diameter) of about 2/3. However, despite the presence of isolated particles observed in zones of high electron-transparency (inset) and owing to projection effects inherent to TEM observations, it is hard to determine whether they are interconnected or not. After annealing at 1070 K for 1 h, the FePt layers are completely broken whereas the vertical periodicity tends to be destroyed (figure 1(c)). The HRTEM micrograph of the annealed specimen (figure 1(d)) reveals that the size of the FePt nanograins increases both in lateral and vertical dimensions and that the distribution is bimodal (inset), i.e. grains with size between 5 and 8 nm are present together with grains exceeding 10 nm. Furthermore, annealing results in the partial graphitization of the carbon matrix as seen from the formation of nanocrystalline graphite-like domains and onion-like structures.

3.2. *Ex situ* GISAXS measurements

To further highlight the differences between the as-deposited and post-annealed $(C/FePt)_{20}$ multilayers, *ex situ* 2D GISAXS patterns collected from a large sample area of about 15 mm^2 are compared in figure 2. In both cases, the vertical beam-stop located around $q_y = 0$ masked the transmitted and specularly reflected intensities. Nevertheless, in the pattern of the as-deposited sample (figure 2(a)), it is immediately

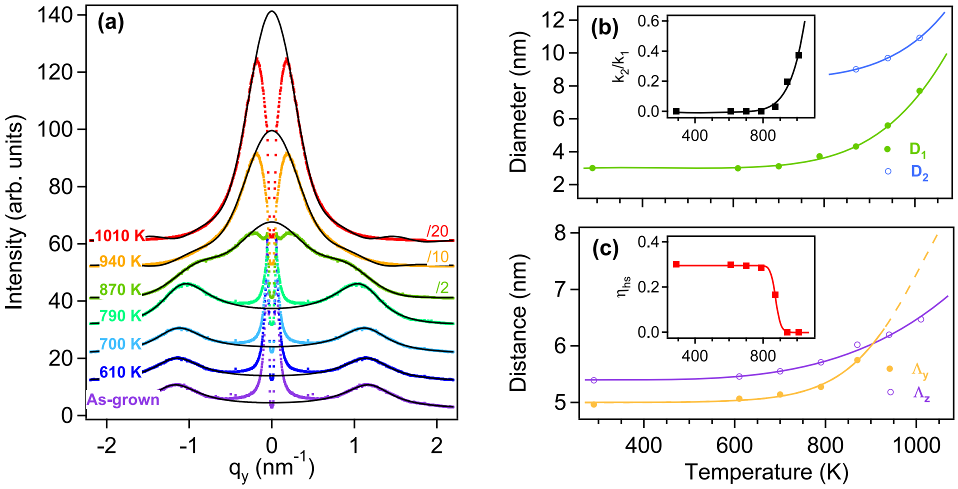

Figure 3. (a) 1D horizontal cross-sections (dots) from 2D GISAXS patterns collected during *in situ* annealing at different temperatures. The solid lines are the best fits using the model described in the text. (b) Temperature dependence of the nanoparticle morphology (D_1, D_2, and k_2/k_1) and (c) organization (Λ_z, Λ_y, and η_{hs}). The solid lines are a guide for the eye.

apparent that there is an intense nonspecular diffuse scattering at low q_y giving rise to three transverse Bragg peaks. Their presence at well-defined q_z-positions (labeled q_{B_1}, q_{B_2}, and q_{B_3}) is typical of a highly periodic system with period $\Lambda_z = 2n\pi/q_{B_n} = 5.4$ nm corresponding to the nominal bilayer thickness ($t_C + t_{FePt}$). Conversely, the absence of transverse Bragg peaks in the 2D GISAXS pattern of the multilayer annealed at 1070 K for 1 h (figure 2(b)) is characteristic of a poor vertical organization of the particles, in agreement with TEM observations (figure 1). Another distinctive feature in figure 2(a) is a coherent small-angle scattering from self-organized nanoparticles [30] giving rise to four diffuse spots centered around $q_y = \pm 1.10\ \mathrm{nm}^{-1}$ and $q_z \approx q_{B_1}/2$ (first order) and $q_z \approx (q_{B_1} + q_{B_2})/2$ (second order). In contrast, the 2D GISAXS pattern of the multilayer annealed at 1070 K for 1 h shows an intense signal close to the origin of the reciprocal space, typical of large uncorrelated particles [31].

3.3. In situ GISAXS measurements

To study in real-time the kinetics of particle growth, $(C/FePt)_{40}$ multilayers were characterized by *in situ* GISAXS measurements under annealing from RT to 1010 K. Figure 3(a) shows a series of 1D horizontal cross-sections performed at $q_z = q_{B_1}/2$ from 2D GISAXS patterns collected during annealing at different temperatures, T_a. It illustrates the progressive transformation of the granular multilayer from a system of small correlated nanoparticles at low T_a ($\leqslant$790 K) to a system of large uncorrelated nanoparticles at higher T_a ($\geqslant$940 K). To obtain further information on the nanoparticle size, interparticle distance and spatial organization from GISAXS measurements, we assumed the scattered intensity $I(\mathbf{q})$ originating from a bimodal distribution of spheroidal particles (as supported by TEM observations, section 3.1) isotropically distributed in a thick carbon layer. $I(\mathbf{q})$ has been decomposed into two independent parts: one from k_1 small correlated nanoparticles with in-plane diameter D_1, in-plane interparticle distance Λ_y, and hard sphere packing fraction η_{hs} (that characterizes the local arrangement of nanoparticles relative to one another [28, 32]), and one from k_2 larger uncorrelated nanoparticles with in-plane diameter D_2. Figures 3(b) and (c) display the evolution of the parameters retrieved from the best fits to the experimental GISAXS data shown in figure 3(a) as a function of T_a. For annealing temperatures between RT and 790 K, only small correlated nanoparticles are present in the granular multilayer ($k_2 = 0$). In this temperature range, their in-plane diameter D_1 increases significantly from 3.0 to 3.7 nm, while the bilayer thickness ($\Lambda_z \approx 5.5$ nm), the in-plane interparticle distance ($\Lambda_y \approx 5.1$ nm), and the in-plane local arrangement of the particles ($\eta_{hs} \approx 0.295$) are subjected to very slight variations (<5%). This indicates that the volume fraction of nanoparticles formed in the as-deposited state is increased by post-annealing. Therefore, we can suggest that significant numbers of Fe and Pt atoms do not participate in the formation of the as-deposited nanoparticles seen by GISAXS and TEM, and that the coarsening of the post-annealed particles first results from thermally activated migration of atoms which were initially dissolved in the matrix. In contrast, for annealing temperatures from 790 up to 1010 K, D_1 and Λ_y increase continuously whereas η_{hs} decreases abruptly to reach zero at $T_a = 940$ K. Furthermore, associated with the coarsening of the nanoparticles with in-plane diameter D_1, and the destruction of the organization, is the progressive formation of many larger uncorrelated nanoparticles with in-plane diameter D_2 varying from 9.0 nm at $T_a = 870$ K to about 11 nm at $T_a = 1010$ K. This phenomenon is progressive, as seen in the gradual increase of k_2/k_1 (inset of figure 3(b)), which represents the ratio of the number of uncorrelated nanoparticles over the number of correlated nanoparticles. In this sense, we can speculate that the bimodal distribution results from the coarsening of the post-annealed particles, which occurs mainly by coalescence phenomena at high temperatures (>790 K). It is also worth noting that in this temperature range, the

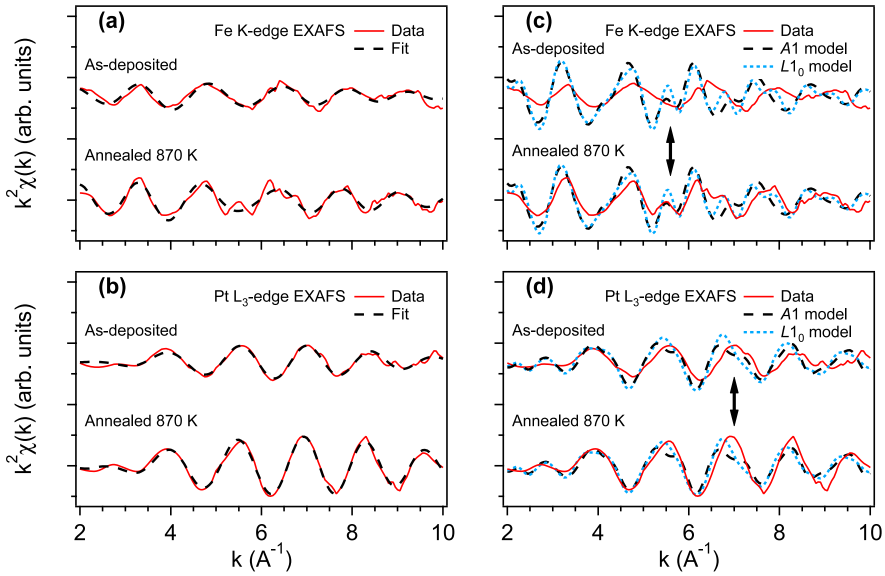

Figure 4. EXAFS spectra at (a) Fe K and (b) Pt L_3 edges of $(C/FePt)_{40}$ multilayers as-deposited and post-annealed at 870 K for 1 h. First shell fits are superposed on the data. Comparison of experimental EXAFS spectra at (c) Fe K and (d) Pt L_3 edges with calculations assuming A1 and $L1_0$ phases. The regions around 5.6 Å^{-1} at the Fe K edge and around 7.0 Å^{-1} at the Pt L_3 edge (indicated by arrows) are very sensitive to the order of the first coordinating atomic shells.

Table 1. Results obtained from the quantitative analysis performed simultaneously on the Pt and Fe EXAFS signals: type and number of nearest neighbors, corresponding distance and mean square relative displacement σ^2.

Sample	Type of neighbors	Coordination number	Distance (Å)	σ^2 (10^{-2} Å^2)
$(C/FePt)_{40}$ multilayer	Fe–Fe	3.6 ± 0.4	2.55 ± 0.03	2.4 ± 0.4
(As-deposited)	Fe–Pt	2.2 ± 0.4	2.56 ± 0.01	1.1 ± 0.2
	Pt–Pt	3.6 ± 0.4	2.67 ± 0.05	1.1 ± 0.6
$(C/FePt)_{40}$ multilayer	Fe–Fe	5.4 ± 0.3	2.66 ± 0.03	3.2 ± 0.4
(Annealed 870 K)	Fe–Pt	4.0 ± 0.3	2.63 ± 0.01	0.9 ± 0.1
	Pt–Pt	5.4 ± 0.3	2.68 ± 0.01	0.7 ± 0.1

partial graphitization of the carbon matrix leads to a significant increase of the bilayer thickness Λ_z [33].

4. Local atomic order and chemical ordering

4.1. Ex situ EXAFS measurements

EXAFS data obtained from $(C/FePt)_{40}$ multilayers as-deposited and post-annealed at 870 K for 1 h are presented in figure 4. EXAFS signals of the as-deposited multilayer measured at both the Fe K and Pt L_3 edges are characteristic of an amorphous-like structure with disordered outer coordination shells. In a first stage, quantitative analysis was performed simultaneously on the Pt and Fe EXAFS signals by using the IFEFFIT and AUTOBK codes [34] to fit the experimental data (figures 4(a) and (b)). The results listed in table 1 reveal that a model including only the first coordination shell leads to a consistent solution at both the Fe K and Pt L_3 edges. For the as-deposited $(C/FePt)_{40}$ multilayer, the structure was expected to be fcc with Pt and Fe atoms randomly distributed over equivalent positions, i.e. six hetero-atomic (Fe–Pt) and six homo-atomic (Fe–Fe or Pt–Pt) neighbors. However, our results show a reduction of the total coordination number N_{tot} to 5.8 (i.e. 3.6 homo-pairs and 2.2 hetero-pairs). Such a decrease of N_{tot} can be explained by the presence of Fe and Pt atoms dissolved in the matrix and by the small particle size. Moreover the large values of mean square relative displacement, σ^2, confirm that the as-deposited nanoparticles are poorly crystallized. After annealing at 870 K for 1 h, coordination numbers rise, whereas σ^2 values associated to Fe–Pt and Pt–Pt distances drop to reach values characteristic of well-crystallized systems. However, the σ^2 value remains large for Fe–Fe pairs, indicating a broad distribution of Fe–Fe distances even after annealing. This can be related to the fact that Pt atoms have a larger atomic radius than Fe atoms, but another possible reason could be the formation of carbon-encapsulated FePt nanoparticles with an amorphous iron-rich interface [35]. It is worth noting that annealing also causes an expansion of the Fe–Fe and Fe–Pt distances, and an increase of the coordination number ratio between the number of hetero-atomic and homo-atomic neighbors from 0.61 to 0.74. However, the ratio remains far from the value of 2 expected for a perfect $L1_0$ phase (8 Fe–Pt and 4 Fe–Fe).

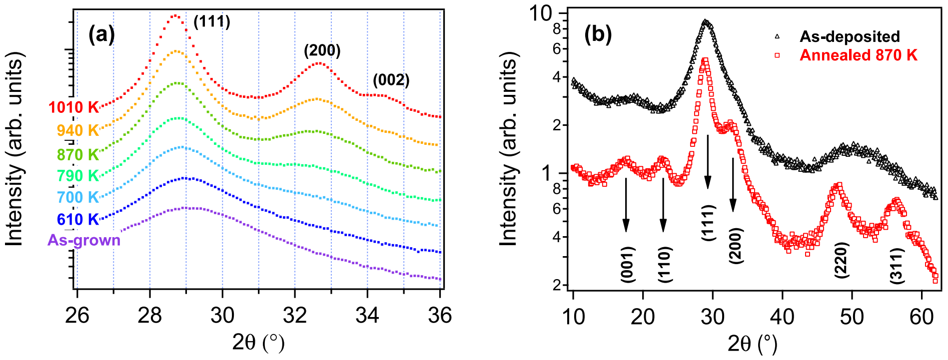

Figure 5. (a) *In situ* GIXRD data for $(C/FePt)_{40}$ multilayers annealed in vacuum. (b) *Ex situ* GIXRD data for $(C/FePt)_{40}$ multilayers as-deposited and post-annealed at 870 K for 1 h.

In order to prove that the structure of our annealed nanoparticles approaches that of the $L1_0$ phase, *ab initio* EXAFS calculations including more coordination shells were performed by FEFF 8 with self-consistent potentials [36]. Theoretical signals resulting from A1 and $L1_0$ clusters are compared with experimental data in figures 4 (c) and (d). Both models do not fit the data perfectly, especially at the Fe K edge due to the strong σ^2 value. However, specific features of the A1 phase fine structure in the region around 7.0 Å^{-1} at the Pt L_3 edge are observed in the data of the as-deposited multilayer. Meanwhile, the calculated $L1_0$ data at both the Fe K edge (around 5.6 Å^{-1}) and Pt L_3 edge (around 7.0 Å^{-1}) match well the experimental data for the post-annealed multilayer. EXAFS measurements thus suggest that thermal annealing induces a transformation from a poorly structured FePt phase to an ordered $L1_0$-like phase. Furthermore, it is important to notice that EXAFS measurements, which are an average over all Fe and Pt atoms, can also detect fractions of oxides or carbides (usually not less than 5%). Nonetheless, x-ray absorption near-edge structures at both the Fe K and Pt L_3 edges are characteristic of metallic binary alloys, indicating that the nanoparticles are well protected from oxidation by the carbon matrix.

4.2. *In situ GIXRD measurements*

In situ GIXRD data presented in figure 5(a) show that the as-deposited film consists of disordered fcc FePt grains with only a very broad (111) peak due to the small size and amorphous-like structure of the grains. However, it may be noticed that its shape is asymmetrical, extending to the higher angle values, which could be explained by the contribution of the (200) peak to the total diffracted intensity. The lattice parameter $a = 3.790$ Å deduced from the position of the (111) Bragg reflection is smaller than the lattice constant of the disordered A1 FePt phase $a_{\text{bulk}} = 3.816$ Å. This lattice contraction of $\sim$0.7% may be attributed to small size effects [37] or to the presence of compressive stress commonly observed in ion-beam sputtered films [38, 39]. Furthermore, the apparent mismatch between the EXAFS and the diffraction local structure ($a_{\text{XRD}} > a_{\text{EXAFS}}$) confirms the important disorder occurring in these materials [40]. As the annealing temperature increases, the (111) peak sharpens due to grain coarsening and its position shifts to lower angle values, which can be related to thermal expansion effects and/or relief of in-plane compressive stress. Beyond $T_a = 790$ K, the (200) reflection becomes clearly visible and shifts to higher angle values as the temperature increases, despite thermal dilatation. At $T_a = 1010$ K the splitting of the (200)–(002) reflections in the GIXRD pattern attests that the $L1_0$ phase has formed. The lattice parameters deduced from the positions of the (200) and (002) Bragg reflections corrected for thermal expansion effects are $a \approx 3.886$ Å and $c \approx 3.700$ Å, which corresponds to a tetragonality ratio c/a of 0.95 close to the bulk $L1_0$ one ($a_{\text{bulk}} = 3.853$ Å, $c_{\text{bulk}} = 3.713$ Å, $c/a = 0.96$).

4.3. *Ex situ XRD measurements*

In order to obtain quantitative information on the chemical order parameter S, additional *ex situ* XRD experiments were carried out on a wider angular range to cover the (001), (110), (200), (002), (220), and (202) Bragg reflections. It is worth noting that from the intensity ratio of the XRD peaks in both Bragg–Brentano and grazing incidence geometries, the FePt grains were indicated to be randomly oriented. In qualitative agreement with the EXAFS and *in situ* GIXRD results, the *ex situ* GIXRD pattern of the as-deposited $(C/FePt)_{40}$ multilayer (figure 5(b)) shows reflections corresponding to a poorly crystallized fcc structure with a lattice parameter $a = 3.790$ Å. However, two bumps located around $2\theta \approx 18°$ and around $2\theta \approx 52°$ are observed. The latter can be interpreted as the merging of the (220), (311), and (222) peaks into one because of an amorphous-like structure of the FePt grains, as suggested by EXAFS measurements. The former might be due to nanometric graphite-like domains present in the carbon matrix or to the formation of poorly crystallized tetragonal FePt grains. Meanwhile, the formation of the ordered $L1_0$ FePt phase characterized by the appearance of the (001) and (110) superstructure peaks is clearly evidenced in the *ex situ* GIXRD pattern of the $(C/FePt)_{40}$ multilayer post-annealed at 870 K for 1 h (figure 5(b)). From the positions of the (001) and (110) reflections, respectively, values of $c \approx 3.610$ Å and $a \approx 3.952$ Å can be determined, which attest to a strong tetragonality of the $L1_0$ FePt phase ($c/a \sim 0.91$) at

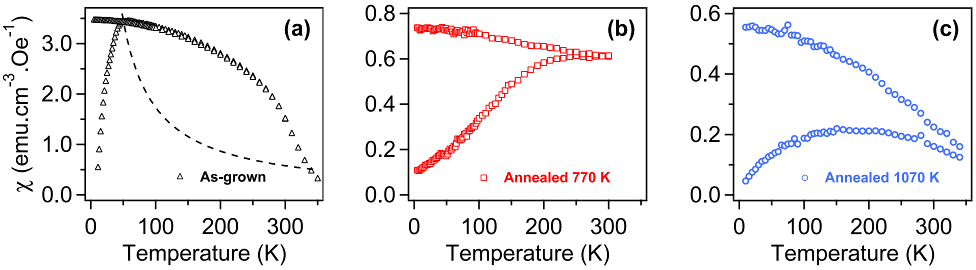

Figure 6. ZFC–FC magnetization curves of (C/FePt)$_{20}$ multilayers: (a) as-deposited multilayer measured in a field of 200 Oe (the dotted line represents the susceptibility given by a Curie-type law), (b) post-annealed at 770 K for 2 h, and (c) post-annealed at 1070 K for 1 h measured in a field of 100 Oe.

$T_a = 870$ K. It is here important to point out that the estimation of the chemical order parameter from the c/a ratio [41] would lead to $S = 2$, which is physically impossible (S may vary between 0 for a fully disordered FePt alloy to 1 for the perfectly ordered alloy). Actually, the a and c values obtained in our study are consistent with the positions found for the (111) and (200) reflections, but do not match that of the (220) and (311) reflections. This suggests that, despite the strong tetragonality of the L1$_0$ FePt phase, only partial chemical ordering has taken place at 870 K and that some FePt grains remain disordered. Therefore the observed (220) and (311) reflections correspond to an average of the diffracted intensity from L1$_0$ ordered and A$_1$ disordered FePt grains. The chemical order parameter S was thus estimated from the ratio of the integrated intensities of the (001) and (110) superstructure peaks versus the (002) and (220) fundamental peaks following the analysis described in [42, 43], and assuming that partial ordering occurred homogeneously within all FePt grains. According to the EXAFS data (see table 1), we also assumed that $\sigma^2_{\mathrm{Fe}} = 2\sigma^2_{\mathrm{Pt}}$. The theoretical integrated intensity ratios I_{001}/I_{002} and I_{110}/I_{220} were fitted to the experimental ones corrected from the Lorentz-polarization contribution. Best-fit values yield $S = 0.54$, $\sigma^2_{\mathrm{Fe}} = 4.2 \times 10^{-2}$ Å^2, and $\sigma^2_{\mathrm{Pt}} = 2.1 \times 10^{-2}$ Å^2. This S value, which is consistent with the data reported in the literature for 5 nm-FePt nanoparticles embedded in carbon [20], confirms that partial ordering takes place at 870 K. The σ^2 values, although relatively high, are also consistent with those derived from the EXAFS analysis (see table 1) and are of the same order of magnitude as those obtained by Gehanno *et al* [44] in epitaxial FePd alloy thin films. Finally, it is worth noting that the full widths at half-maximum determined from the (001) superstructure and (200) fundamental reflections are ∼4° and ∼2°, respectively, which means that the in-plane coherency length of the ordered domains is half that of the disordered ones. Taking into account that the grain size distribution is bimodal, it may be inferred that L1$_0$ ordering first takes place in the smallest grains (<4 nm) as already suggested by Christodoulides *et al* [20].

5. Magnetic properties

The temperature dependence of the magnetic susceptibility $\chi(T)$ collected both after zero-field cooling (ZFC) and field cooling (FC) is displayed in figure 6 for as-deposited and post-annealed (C/FePt)$_{20}$ multilayers. As commonly observed in granular magnetic systems [45, 46], the ZFC curve of the as-deposited multilayer exhibits a peak in magnetization at $T_B \sim 50$ K, the blocking temperature below which the magnetization of most of the nanoparticles is blocked. In addition, as expected for superparamagnetic systems, the ZFC and the FC curves show strong irreversibility below T_B. However, although the magnetization exhibits a reversible behavior above T_B, $\chi(T)$ cannot be described by a Curie-type law (i.e. $1/\chi$ is not linear in T). Furthermore, as reported in a previous paper [33], the magnetization curves $M(H)$ of the as-deposited multilayer measured above T_B cannot be fitted by a Langevin function. These results suggest that strong interactions exist between as-deposited FePt nanoparticles due to their proximity.

After annealing at 770 K for 2 h, the ZFC–FC curve of the multilayer displayed in figure 6(b) reveals an obvious irreversibility below $T_B \sim 250$ K. Besides, the magnetization curve $M(H)$ measured at RT (figure 7(a)) shows a soft magnetic feature with zero remanence and coercivity, suggesting that the nanoparticles are thermally unstable, i.e. they are in the superparamagnetic state. Under the assumption of weak interparticle interactions, the magnetization curve $M(H)$ of such a superparamagnetic system can be described by a weighted sum of Langevin functions that takes into account a distribution of magnetic moments due to the particle size distribution $N(V)$:

$$M(H) = M_s \int_0^{\infty} \left[\coth(x) - \frac{1}{x}\right] N(V)\,\mathrm{d}V, \qquad (1)$$

where $x = M_s V H / k_B T$, M_s is the saturation magnetization, k_B is the Boltzmann constant, and V is the particle volume. Assuming a Gaussian distribution of spherical particles with diameter D, the fit to the experimental data yields an average diameter $\langle D \rangle = 6.0$ nm and a standard deviation $\sigma = 1.5$ nm. This magnetic size $\langle D \rangle$ is found to be slightly higher than the structural size determined by *ex situ* GISAXS ($D_1 = 4.0$ nm and $D_2 = 5.7$ nm with $k_2/k_1 = 0.04$), suggesting that the magnetic particles are weakly coupled. In figure 6(c), the ZFC curve of the multilayer annealed at 1070 K for 1 h displays a very broad peak at ∼190 K. However, most of the particles remain blocked at 350 K so that the film shows hard magnetic properties even at RT.

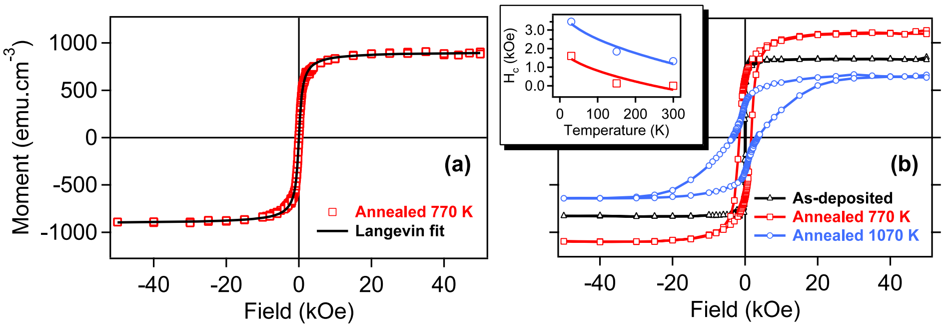

Figure 7. (a) Hysteresis loop of the $(C/FePt)_{20}$ multilayer post-annealed at 770 K for 2 h measured at RT. The solid line is the best fit to the experimental data using equation (1). (b) Hysteresis loops of as-deposited and post-annealed $(C/FePt)_{20}$ multilayers measured at 30 K. Temperature dependence of the coercivity is shown in the inset (the solid lines are the best fits to the experimental data using equation (2)).

Table 2. Magnetic properties of as-deposited and post-annealed $(C/FePt)_{20}$ multilayers determined from hysteresis loops measured at various temperatures. H_c: coercivity in Oe; M_r/M_s: remanence ratio; μ_{at}/μ_B: average magnetic moment per atom (including both Fe and Pt atoms) in units of Bohr magneton.

	H_c (Oe)			M_r/M_s			μ_{at}/μ_B		
	300 K	150 K	30 K	300 K	150 K	30 K	300 K	150 K	30 K
As-deposited	19	14	121	0.29	0.61	0.71	0.66	1.09	1.24
Annealed 770 K	0	132	1603	0	0.12	0.57	1.33	1.57	1.65
Annealed 1070 K	1325	1842	3435	0.30	0.42	0.56	0.66	0.88	0.97

Hysteresis loops of the as-deposited and post-annealed $(C/FePt)_{20}$ multilayers were measured at 300, 150, and 30 K in order to determine the coercivity, H_c, the average magnetic moment per atom (including both Fe and Pt atoms), μ_{at}, and the remanence ratio, M_r/M_s, of the films. The corresponding values are listed in table 2, while magnetization curves $M(H)$ measured at 30 K are shown in figure 7(b) as a typical example. From these measurements, the temperature dependence of H_c is obtained, which is expected to behave according to equation (2) for superparamagnetic systems [47]:

$$H_c(T) = H_0\left(1 - \sqrt{\frac{T}{T_B}}\right), \qquad (2)$$

where H_0 is the zero temperature (intrinsic) coercivity and T_B is the blocking temperature. The solid lines in the inset of figure 7 are fits of equation (2) to the experimental data from which the zero temperature coercivity and the blocking temperature are determined to be $H_0 = 2.2$ kOe and $T_B = 250$ K for the multilayer post-annealed at 770 K and $H_0 = 4.3$ kOe and $T_B = 568$ K for the multilayer post-annealed at 1070 K, respectively. It is interesting to note that the T_B value obtained for the multilayer annealed at 770 K is in excellent agreement with the value determined from the ZFC–FC curve. Furthermore, both H_0 and T_B increase with T_a because of the gradual transformation of the soft fcc FePt phase to the hard fct FePt phase. For spherical particles the rotational energy barrier to alignment is given by the magnetic anisotropy energy per unit volume K multiplied by the particle volume V. For SQUID measurements, the blocking temperature should roughly satisfy the relationship

$$T_B = \frac{K\langle V\rangle}{25k_B}. \qquad (3)$$

Using the $\langle V\rangle$ value determined from the Langevin fit displayed in figure 7(a), we calculate a magnetic anisotropy energy $K = 7.6 \times 10^6$ erg cm^{-3} for the multilayer post-annealed at 770 K for 2 h. This K value is found to be one order of magnitude smaller than the magnetocrystalline anisotropy energy of the FePt binary alloy with $L1_0$ phase ($K_1 = 7 \times 10^7$ erg cm^{-3}) [48], but one order of magnitude higher than the effective magnetic anisotropy estimated for FePt nanoparticles with A1 phase ($K_{eff} = 3.6 \times 10^5$ erg cm^{-3}) [26]. This might be due to incomplete $L1_0$ ordering at this annealing temperature as observed by XRD ($S = 0.54$). On the other hand, the K value of the multilayer post-annealed at 1070 K for 1 h derived from equation (3) using the $\langle V\rangle$ value determined by GISAXS is decreased to $K = 4.5 \times 10^6$ erg cm^{-3}. It can also be seen that a shoulder tends to develop in the magnetization curve near $H = 0$. These results suggest the presence of a soft magnetic phase that is not exchange coupled to the hard phase. The most likely explanation is that annealing at 1070 K causes chemical interaction of FePt layers with the Si substrate as revealed unambiguously by complementary RBS and energy filtered TEM experiments [33].

The variations of the remanence ratio M_r/M_s gathered in table 2 also provide interesting information since the Stoner–Wohlfarth model predicts a value of 0.5 for noninteracting single domain particles with easy axes randomly oriented [49]. At 300 K, the remanence ratio of the as-deposited and post-annealed multilayers is smaller than 0.5 because of the existence of superparamagnetic particles and/or dipolar interactions. A general trend is that M_r/M_s increases as T decreases due to the gradual blocking of the FePt nanoparticles. However, while M_r/M_s reaches $\sim$0.5 for post-annealed multilayers at 30 K, a value of 0.71 is found for the as-deposited multilayer, thus confirming that strong exchange coupling exists between magnetic particles.

The last point to discuss is the evolution of the average magnetic moment per atom μ_{at} upon thermal annealing. As seen in table 2, the μ_{at} value of the as-deposited multilayer determined from the hysteresis loop measured at 30 K (figure 7(b)) is 1.24 μ_B, which is less than the value of 1.54 μ_B expected for disordered fcc FePt [28]. This reduction may be due to the presence of a significant amount of Fe and Pt atoms dissolved in the matrix, as revealed by the GISAXS measurements. A further reason might be attributed to the presence of carbon atoms in the FePt phase or to reduced moments for the atoms at the surface of the nanoparticles resulting in a magnetic dead layer as suggested by the EXAFS measurements. After annealing at 770 K for 2 h, the average magnetic moment per atom rises to $\mu_{at} = 1.65$ μ_B at 30 K, which is approaching the bulk value of 1.71 μ_B for L1_0 FePt. This result confirms not only that partial L1_0 ordering occurs, but also that Fe and Pt atoms previously incorporated in the carbon matrix precipitate upon annealing. However, although H_0 and T_B increase steadily with T_a because of the progressive L1_0 ordering of the FePt nanoparticles, the diffusion of Fe atoms into the substrate at 1070 K [7, 33, 50] leads to a strong decrease of the μ_{at} value to 0.97 μ_B at 30 K.

6. Conclusion

We have investigated the growth kinetics, chemical ordering, and magnetic properties of carbon-encapsulated FePt nanoparticles subjected to thermal annealing by combining *ex situ* and *in situ* measurements. HRTEM and GISAXS show that the as-deposited granular films are composed of isolated FePt nanoparticles of approximately 3 nm in size and surrounded by an amorphous carbon matrix. Our structural data provide evidence that coarsening of the post-annealed particles first takes place mainly through collecting Fe and Pt dissolved in the matrix. At temperatures above 870 K, particles combine to form larger entities by coalescence while carbon atoms precipitate to form graphite-like nanostructures. EXAFS and XRD demonstrate that the FePt nanoparticles, which are well protected from oxidation, undergo a gradual phase transition from a poorly crystallized fcc structure (disordered) to a fct structure (ordered) under annealing. SQUID magnetometry reveals that this phase transition causes magnetic hardening characterized by a strong enhancement of the blocking temperature and coercivity. Anomalous variations of saturation magnetization and magnetocrystalline anisotropy energy at high annealing temperatures (∼1070 K) are ascribed to chemical interaction of Fe atoms with the Si substrate. Thus a close relationship exists between the structural and magnetic properties of these carbon-encapsulated FePt nanoparticles, which may be tuned using appropriate annealing conditions. In that sense, the use of dedicated *ex situ* and *in situ* techniques provides valuable information for investigating chemically ordered magnetic binary alloys in nanoparticle form that present a strong potential for future magnetic recording media.

Acknowledgments

The authors thank P Guérin for his help during the preparation of the C/FePt multilayers. We are grateful to M-F Denanot for performing the HRTEM characterizations. We acknowledge the assistance of O Lyon and E Welter during the GISAXS and EXAFS experiments at LURE and HASYLAB.

References

[1] Weiss N, Kren T, Epple M, Rusponi S, Baudot G, Rohart S, Tajeda A, Repain V, Rousset S, Ohresser P, Scheurer F, Bencok P and Brune H 2005 *Phys. Rev. Lett.* **95** 157204
[2] Liou S H, Liu Y, Malhotra S S, Yu M and Sellmyer D J 1996 *J. Appl. Phys.* **79** 5060
[3] Sun S, Murray C B, Weller D, Folks L and Moser A 2000 *Science* **287** 1989
[4] Kaitsu I, Inomata A, Okamoto I and Shinohara M 1998 *IEEE Trans. Magn.* **34** 1591
[5] Ichihara K, Kikitsu A, Yusu K, Nakamura F and Ogiwara H 1998 *IEEE Trans. Magn.* **34** 1603
[6] Luo C P and Sellmyer D J 1999 *Appl. Phys. Lett.* **75** 3162
[7] Kuo C M and Kuo P C 2000 *J. Appl. Phys.* **87** 419
[8] Watanabe M, Masumoto T, Ping D H and Hono K 2000 *Appl. Phys. Lett.* **76** 3971
[9] Ping D H, Ohnuma M, Hono K, Watanabe M, Isawa T and Masumoto T 2001 *J. Appl. Phys.* **90** 4708
[10] Luo C P, Liou S H, Gao L, Liu Y and Sellmyer D J 2000 *Appl. Phys. Lett.* **77** 2225
[11] Yan M L, Zeng H, Powers N and Sellmyer D J 2002 *J. Appl. Phys.* **91** 8471
[12] Chen S C, Kuo P C, Lie C T and Hua J T 2001 *J. Magn. Magn. Mater.* **236** 151
[13] Karanasos V, Panagiotopoulos I, Niarchos D, Okumura J and Hadjipanayis G C 2001 *J. Magn. Magn. Mater.* **236** 234
[14] Sajurai R, Yamamoto Y, Chen C, Hashimoto M, Shi J, Nakamura Y and Nittono O 2004 *Thin Solid Films* **459** 208
[15] Takahashi Y K, Ohkubo T, Ohnuma M and Hono K 2003 *J. Appl. Phys.* **93** 7166
[16] Christodoulides J A, Huang Y, Zhang Y, Hadjipanayis G C, Panagiotopoulos I and Niarchos D 2000 *J. Appl. Phys.* **87** 6938
[17] Daniil M, Farber P A, Okumura H, Hadjipanayis G C and Weller D 2002 *J. Magn. Magn. Mater.* **246** 297
[18] Delaunay J J, Hayashi T, Tomita M, Hirono S and Umemura S 1997 *Appl. Phys. Lett.* **71** 3427
[19] Yu M, Liu Y, Moser A, Weller D and Sellmyer D J 1999 *Appl. Phys. Lett.* **75** 3992
[20] Christodoulides J A, Bonder M J, Huang Y, Zhang Y, Stoyanov S, Hadjipanayis G C, Simopoulos A and Weller D 2003 *Phys. Rev.* B **68** 054428
[21] Perumal A, Ko H S and Shin S C 2003 *Appl. Phys. Lett.* **83** 3326
[22] Xu Y, Yan M L, Zhou J and Sellmyer D J 2005 *J. Appl. Phys.* **97** 10J320
[23] Mi W B, Liu H, Li Z Q, Wu P, Jiang E Y and Bai H L 2005 *J. Appl. Phys.* **97** 124303
[24] Hayashi T, Hirono S, Tomita M and Umemura S 1996 *Nature* **381** 772
[25] Babonneau D, Briatico J, Petroff F, Cabioc'h T and Naudon A 2000 *J. Appl. Phys.* **87** 3432
[26] Rellinghaus B, Stappert S, Acet M and Wassermann E F 2003 *J. Magn. Magn. Mater.* **266** 142
[27] Takahashi Y K, Koyama T, Ohnuma M, Ohkubo T and Hono K 2004 *J. Appl. Phys.* **95** 2690
[28] Thomson T, Lee S L, Toney M F, Dewhurst C D, Ogrin F Y, Oates C J and Sun S 2005 *Phys. Rev.* B **72** 064441

[29] Barradas N P, Alves E and Babonneau D 2004 *Nucl. Instrum. Methods Phys. Res.* B **219/220** 919
[30] Naudon A, Babonneau D, Petroff F and Vaurès A 1998 *Thin Solid Films* **319** 81
[31] Babonneau D, Camelio S, Girardeau T, Jaouen M and Lyon O 2003 *J. Appl. Crystallogr.* **36** 430
[32] Babonneau D, Pailloux F, Eymery J P, Denanot M F, Guérin P, Fonda E and Lyon O 2005 *Phys. Rev.* B **71** 035430
[33] Babonneau D, Pailloux F, Abadias G, Petroff F, Barradas N P and Alves E 2007 *Rev. Adv. Sci. Mater.* **15** 198
[34] Newville M 2001 *J. Synchrotron Radiat.* **8** 322
[35] Delalande M, Marcoux P R, Reiss P and Samson Y 2007 *J. Mater. Chem.* **17** 1579
[36] Ankudinov A L, Ravel B, Rehr J J and Conradson S D 1998 *Phys. Rev.* B **58** 7565
[37] Henry C R 1998 *Surf. Sci. Rep.* **31** 231
[38] Windischmann H 1992 *Crit. Rev. Solid State Mater. Sci.* **17** 547
[39] Debelle A, Abadias G, Michel A and Jaouen C 2004 *Appl. Phys. Lett.* **84** 5034
[40] Moscovici J, Rougier A, Laruelle S and Michalowicz A 2006 *J. Chem. Phys.* **125** 124505
[41] Christodoulides J A, Farber P, Daniil M, Okomura H, Hadjipanayis G C, Skumryev V, Simopoulos A and Weller D 2001 *IEEE Trans. Magn.* **37** 1292
[42] Cebollada A, Farrow R F C and Toney M F 2002 *Magnetic Nanostructures* ed H S Nalwa (Stevenson Ranch, CA: American Scientific Publishers)
[43] Warren B E 1990 *X-ray Diffraction* (New York: Dover)
[44] Gehanno V, Revenant-Brizard C, Marty A and Gilles B 1998 *J. Appl. Phys.* **84** 2316
[45] Chien C L 1991 *J. Appl. Phys.* **69** 5267
[46] Wang J Q and Xiao G 1994 *Phys. Rev.* B **49** 3982
[47] Kneller E F and Luborski F E 1963 *J. Appl. Phys.* **34** 656
[48] Ivanov O A, Solina L V, Demshina V A and Magat L M 1973 *Phys. Met. Metallogr.* **35** 81
[49] Stoner E C and Wohlfarth E P 1948 *Phil. Trans. R. Soc.* A **240** 599
[50] Thomson T, Terris B D, Toney M F, Raoux F, Baglin J E E, Lee S L and Sun S 2004 *J. Appl. Phys.* **95** 6738